



Monodisperse Porous Carbon Nanospheres with Ultra-High Surface Area for Energy Storage in Electrochemical Capacitors

Noel Díez,^{*[a]} Marta Sevilla,^[a] Alba Fombona-Pascual,^[a] and Antonio B. Fuertes^[a]

Highly porous carbon nanoparticles are very suitable materials for supercapacitor electrodes due to their combination of large surface area for ion adsorption and short pathways for fast ion diffusion. Herein we describe the synthesis of highly porous carbon nanospheres ($d=90\text{ nm}$) by a simple strategy that involves the preparation of monodisperse nanoparticles by the oxidative polymerization of pyrrole, followed by their direct chemical activation with KHCO_3 . The morphology of the nanospheres is well retained after activation, and the inorganic impurities are removed by a simple washing step with water. The porous nanospheres possess a high electrical conductivity and specific surface areas exceeding $3000\text{ m}^2\text{ g}^{-1}$ due to their high content of micropores and small mesopores ($<4\text{ nm}$).

Their highly developed and readily available porosity make these materials promising for use as supercapacitor electrodes. In the aqueous $1\text{ M H}_2\text{SO}_4$ electrolyte, the porous nanospheres reach a capacitance of 262 F g^{-1} and withstand an ultrahigh current density of 80 A g^{-1} maintaining a capacitance above 100 F g^{-1} . In the organic $1\text{ M TEABF}_4/\text{AN}$ and EMImTFSI/AN electrolytes, the nanoparticles reach 175 and 155 F g^{-1} , and the supercapacitors could be cycled up to 50 A g^{-1} delivering 30 Wh kg^{-1} at a power density of 20 kW kg^{-1} and 31 Wh kg^{-1} at a power density of 31 kW kg^{-1} , respectively. These results demonstrate the potential of these nanoparticles for energy storage applications.

1. Introduction

Carbon materials have acquired great importance as essential components in electrochemical energy storage and conversion devices.^[1–4] There is an increasing interest and growing demands for these materials, given their low cost, high chemical resistance and good thermal and electrical conductivities. In addition, they have the capacity to adopt a great variety of structural and physicochemical characteristics (from a certain graphitic order to well-developed and tunable pore structures, heteroatom doping, particle size, and tailored morphologies), which make them well-suited to a wide variety of practical applications.

Among the diversity of carbon materials, carbon nanostructures (e.g., nanotubes, nanofibers, graphene, nanosheets, nanospheres, etc.) have generated a great interest for electrochemical applications, driven by some of their specific characteristics including good dispersibility and mixing, large external surface areas for chemical modification or short diffusional pathways. In this regard, very small carbon particles ($<1\text{ }\mu\text{m}$), including carbon blacks, have attracted substantial attention as

electrode materials in electrochemical energy storage and conversion devices such as electrochemical capacitors,^[5] batteries (i.e., lithium-ion, sodium-ion, potassium-ion, zinc-air, and lithium-sulfur),^[6] hybrid capacitors,^[7,8] and also as electrocatalysts in fuel-cells.^[9] For many electrochemical applications, such as supercapacitors, carbon materials must also possess an extensive pore development with a large specific surface area and a controlled pore size that guarantees a high energy density.^[10] Moreover, the achievement of high power density requires high mass transfer rates, which can be accomplished by using carbon nanoparticles with short diffusional pathways. Therefore, the use of carbon materials that combine a high surface area, controlled pore size, and critical dimensions $\leq 100\text{ nm}$ is, in principle, highly advantageous for supercapacitors and other energy storage systems.

Sub-micrometric porous carbon particles with a spherical morphology can be produced from different types of polymeric materials by using two main synthesis strategies. One is based on templating techniques that imply the formation of spherical particles. This approach combines, at the nanoscale level, a polymeric phase with inorganic (hard template methods with silica)^[11–14] or organic (soft template methods with thermally unstable compounds)^[14–16] substances. Another strategy comprises the physical/chemical activation of polymeric spheres made up of thermosetting polymers (i.e., phenolic resins, saccharide-based hydrochar, polypyrrole, polyacrylonitrile, etc.), which can be produced following different methodologies, including the Stöber method,^[17] the benzoxazine approach,^[18,19] emulsion-polymerization,^[20,21] as well as hydrothermal carbonization.^[22]

[a] Dr. N. Díez, Dr. M. Sevilla, A. Fombona-Pascual, Prof. A. B. Fuertes
Instituto de Ciencia y Tecnología del Carbono
INCAR-CSIC, Francisco Pintado Fe, 26. 33011 Oviedo, Spain
E-mail: noel@incar.csic.es

 Supporting information for this article is available on the WWW under
<https://doi.org/10.1002/batt.202100169>

 © 2021 The Authors. *Batteries & Supercaps* published by Wiley-VCH GmbH.
This is an open access article under the terms of the Creative Commons Attribution Non-Commercial License, which permits use, distribution and reproduction in any medium, provided the original work is properly cited and is not used for commercial purposes.

The conversion of polymeric spheres into porous carbon is usually carried out by a two-step process that first involves the carbonization of polymeric material and, subsequently, a heat-treatment with an oxidant substance that serves as activating agent. This scheme has been used by several authors with gaseous agents that can produce a physical activation, such as carbon dioxide or steam.^[23] KOH is a chemical activating agent that has been widely used for direct activation of raw polymer or biomass precursors. Unfortunately, it has been abundantly shown that KOH acts as a flux agent, causing the melting and coalescence of the precursor particles. Thus, it produces irregular porous carbon particles with conchoidal cavities, irrespective of the initial particle morphology.^[24–26] To circumvent this problem, several authors have implemented a two-step process that involves KOH activation of the pre-carbonized polymer. However, this strategy limits pore development.^[27,28] We have observed that other activating agents such as Na₂S₂O₃ also induce polymer melting and then, a pre-carbonization step is also required.^[29,30] By contrast, certain activating agents such as K₂CO₃, KHCO₃,^[24] or potassium oxalate^[31] can be directly used with polymer spheres in a one-step process to produce porous carbon spheres that maintain their shape. This approach notably simplifies the synthesis and yields porous materials with an extensive pore development.

Whereas the synthesis of sub-micrometric porous carbon spheres with diameters in the 0.1–1 µm range has been widely studied,^[11,17,24,32–35] the production of highly porous carbon nanospheres (diameter $d \leq 100$ nm) (PCNSs) by using effective, easy, and sustainable procedures is a significant target that still has not been adequately addressed. Ideally, the strategy to accomplish this objective should be focussed on the design of one-step activation processes based on non-corrosive chemical activating agents. We have verified the feasibility of this strategy in the case of sub-micrometric hydrochar spheres ($d \sim 0.4$ µm) directly activated with KHCO₃.^[24]

Polypyrrole is an N-rich polymer that can be easily produced in water through oxidative polymerization of pyrrole, a water-soluble monomer. This polymer has been widely used as a carbon precursor owing to its high carbon yield (>50%) and also because of its versatility to generate, with the aid of appropriate structure-directing agents, a variety of polymer nanostructures including nanofibers,^[36,37] nanotubes,^[38,39] or nanospheres.^[40–44] In particular, the synthesis of polypyrrole nanospheres (diameter ≤ 100 nm) can be accomplished by means of simple procedures, which makes this precursor suitable for the production of porous carbon derivatives. In this respect, we have reported the synthesis of porous carbon nanoparticles through a two-step process that involves the activation of pre-carbonized polypyrrole nanospheres with Na₂S₂O₃.^[30] Herein, we present an easy synthesis pathway to produce highly porous carbon nanospheres in a single step. Such PCNSs are synthesized through the direct activation of polypyrrole nanospheres with KHCO₃ and offer two significant characteristics: i) a monodisperse size distribution with $d \sim 100$ nm and ii) ultra-high BET surface areas ($> 3000\text{ m}^2\text{ g}^{-1}$) associated to micropores and small mesopores (< 4 nm). For the reasons previously disclosed, these properties make the

PCNSs good candidates for implementation in electrical double layer capacitor (EDLC) systems. Accordingly, we analysed their behaviour as electrodes in electrochemical capacitors using three different types of electrolytes (i.e., H₂SO₄, TEABF₄/AN, and EMImTFSI/AN). By virtue of their highly developed and readily accessible pore structure, the porous nanospheres achieved high capacitance and preserved an excellent electrochemical response at high power demand.

2. Results and Discussion

2.1. Synthesis Strategy of Polymer and Porous Carbon Nanospheres

The synthesis of polypyrrole nanospheres was performed in aqueous media by the oxidative polymerization of pyrrole with FeCl₃ (oxidant), and in the presence of a stabilizer to block the precipitation and coalescence of the generated polymeric particles. A scheme illustrating the synthesis of polymer nanospheres and PCNSs is shown in Figure 1. Following the strategy proposed by Jang et al.,^[41,42,44] we used a water-soluble polymer (polyvinyl alcohol, PVA) as the stabilizing agent, which combines with the oxidant cation (Fe³⁺) to create a PVA/Fe³⁺ complex that serves as the reactive site where the polymerization and growth of polypyrrole nanospheres occurs. These polymer nanospheres are monodisperse with a mean diameter of 112 nm (standard deviation: 19 nm), as indicated in the SEM image (Figure 2a).

The polymer nanospheres were activated simply by heating the polypyrrole/KHCO₃ mixture at a temperature $\geq 750^\circ\text{C}$ under an inert atmosphere (samples were labelled as ANP-X, X being the activation temperature). Thus, in a single thermal treatment, both the carbonization of the polymer and the generation of internal pores through the oxidation reactions caused by KHCO₃ take place, as we have already discussed.^[24,45] In brief, at ~ 150 – 200°C , KHCO₃ decomposes to potassium carbonate (2 KHCO₃ \rightarrow K₂CO₃ + CO₂ + H₂O) that, at higher temperatures ($> 700^\circ\text{C}$), oxidizes the carbonaceous matter (K₂CO₃ + 2 C \rightarrow 2 K + 3 CO).^[46,47] This oxidation reaction, together with the intercalation of the generated K vapours between the graphene layers, causes the formation of numerous internal nanovoids (micropores). At higher temperatures ($> 850^\circ\text{C}$) the potassium carbonate slowly decomposes (K₂CO₃ \rightarrow K₂O + CO₂) and the generated products react with carbon through two oxidation reactions (CO₂ + C \rightarrow 2 CO and K₂O + C \rightarrow 2 K + CO) that lead to the formation of new micropores and the enlargement of those previously formed. At this point, it needs to be mentioned that, as the decomposition of N-groups takes place in the presence of potassium salts, oxidizing substances (i.e., KCNO) that also act as activating agents might be formed, enhancing thereby pore development as we have already discussed.^[48–50] The overall process gives rise to a porous carbon material containing a large number of micropores and a limited amount of small mesopores. Once the activation has concluded, the PCNSs can be collected just by removing the

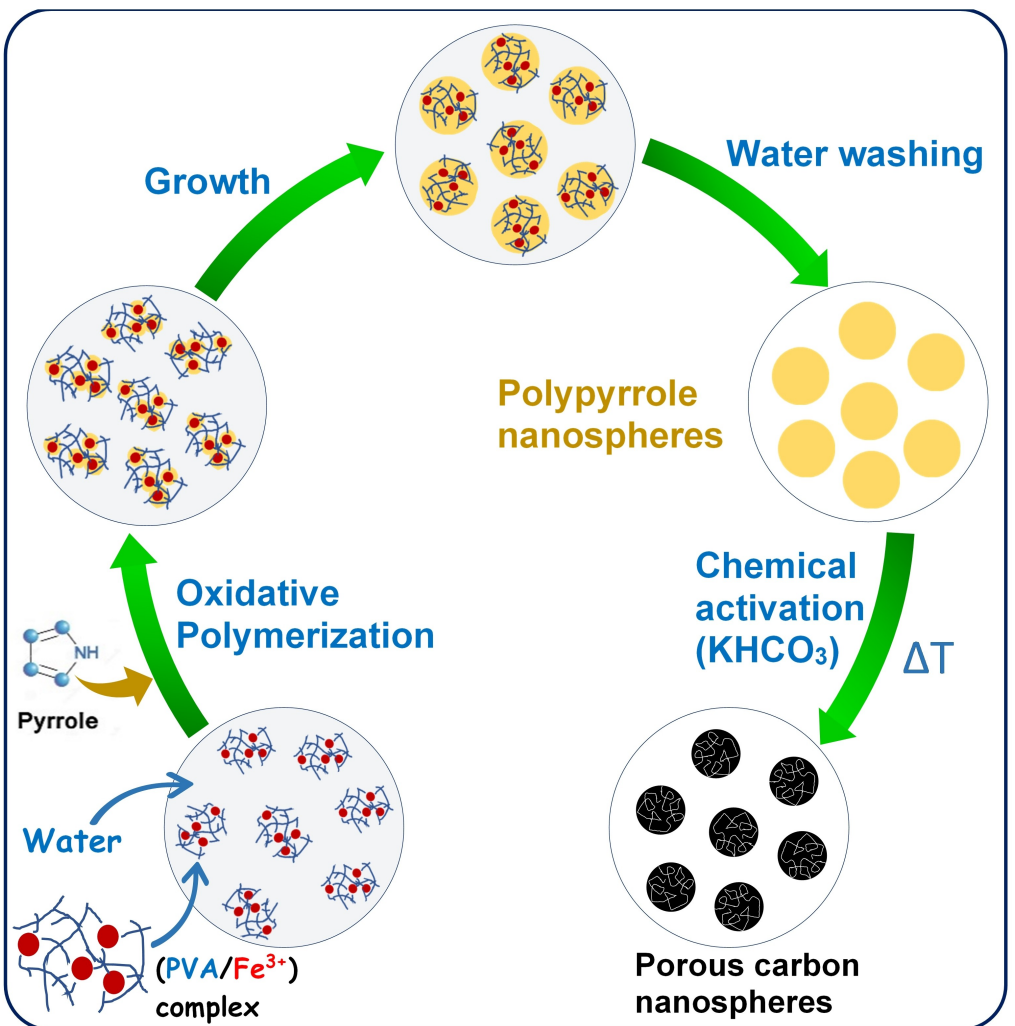


Figure 1. Synthesis of polypyrrole nanospheres and their activation with KHCO₃ to form PCNSs.

inorganic impurities by water washing, which is desirable for an easy and sustainable synthesis.

2.2. Morphology and Physicochemical Properties of the Porous Carbon Nanoparticles

The morphology and microstructure of the carbon materials were examined by scanning electron microscopy (SEM) and transmission electron microscopy (TEM). The carbon nanospheres obtained just by carbonization at 800 °C have a uniform diameter of 89 nm (standard deviation = 11 nm). This value is 21 % lower than that of the polymer nanoparticles due to the matter loss typical of the carbonization process (the carbonization yield is of 54%). The carbonized nanoparticles retain their spherical morphology and remain uncoalesced (Figure 2b). The carbonized nanoparticles are nonporous and, consequently, have a low BET surface area of 60 m² g⁻¹, which corresponds to the external surface area. Direct activation of the polymeric nanospheres with KHCO₃ conducts to non-agglomerated carbon particles that retain the spherical

morphology, as shown in the SEM (Figures 2c and S1) and TEM images (Figure 2d). The SEM and TEM images also reveal that the PCNSs have narrow particle size distributions with a diameter of 90–97 nm (see Table 1). By comparison with the carbonized sample CNP-800, it is clear that the activation does not involve further reduction of the diameter of the nanoparticles, which suggests that reaction with potassium bicarbonate to generate porosity occurs uniformly across the nanoparticles without causing any collapse of the pore structure. A close inspection of the activated samples by TEM reveals that the PCNSs consist of randomly oriented graphene-like layers enclosing narrow micropores (Figures 2e and f, S2). This carbon structure is consistent with the XRD patterns containing hardly visible (002) and (100) bands (Figure S3a). The Raman spectra corresponding to the activated samples are shown in Figure S3b. Its quantitative analysis, after deconvolution into the D*, D, D'' and G bands, reveals a slight decrease of the integrated I_D/I_G ratio, from 2.48 to 2.33, with the increase of the activation temperature from 750 to 950 °C. Also, the signals corresponding to the G and D bands become a little narrower at higher activation temperatures, the FWHM (Full Width at

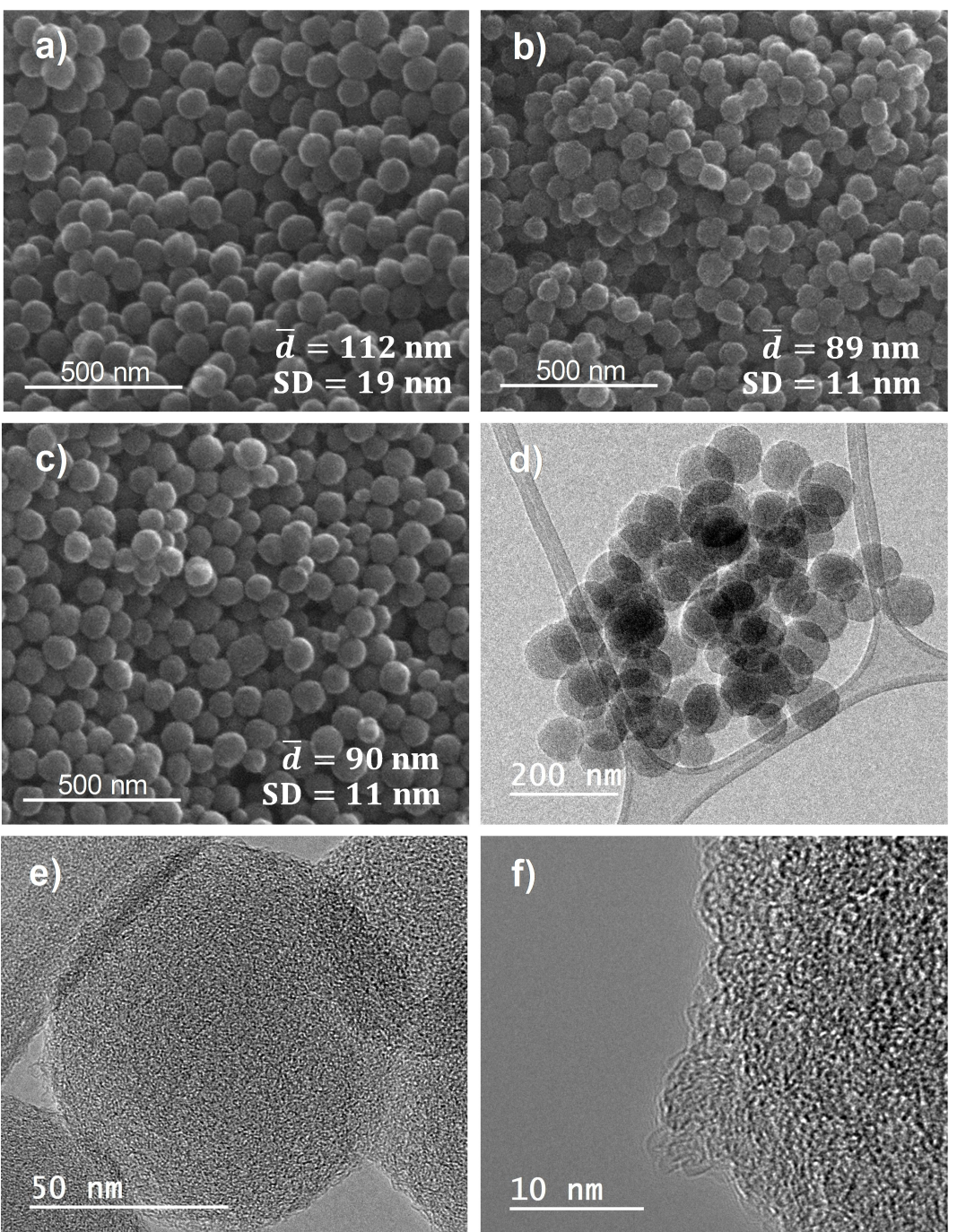


Figure 2. SEM images of a) polypyrrole nanospheres, b) carbonized polypyrrole nanospheres (800°C), and c) activated polypyrrole nanospheres (activation temperature of 800°C). d–f) TEM microphotographs of the ANP-750 porous nanospheres.

Half Maximum) values decreasing from 95 to 79 cm^{-1} for the G band and from 222 to 116 cm^{-1} for the D band, respectively. Both observations are indicative of certain increase of the ordering degree in the carbonaceous structure, likely due to the loss of heteroatoms and in-plane defects, as well as the growth of the aromatic clusters.

Further analysis of the textural properties of PCNSs was carried out by nitrogen physisorption. The nitrogen sorption isotherms and the pore size distributions of the PCNSs are presented in Figure 3a and b, respectively. The isotherm

profiles displayed in Figure 3a are of type Ib, which reveals that the internal porosity is made up of small pores (i.e., micropores and small mesopores). The large nitrogen uptake observable at $p/p_0 > 0.9$ can be attributed to the capillary condensation in the interparticle voids. Furthermore, there is a broadening of the knee of the isotherms as the activation temperature increases from 750 to 950°C , which indicates a widening of the pore size. These conclusions are confirmed by the pore size distributions presented in Figure 3b, which are bimodal, with one pore system composed of narrow micropores of around 0.8 nm and

Table 1. Physico-chemical properties of the porous carbon nanospheres.

Sample code	Activation temperature [°C]	Carbon yield [%]	Diameter of PCNSs ^[a] [nm]	Textural properties		Electrical conductivity [S cm ⁻¹]	Packing density [g cm ⁻³]	Electrode density [g cm ⁻³]
CNP-800	–	54	89 (11)	60	0.08	0.01 (0.01)	3.1	1.10
ANP-750	750	31	93 (9)	3040	1.40	1.16 (0.62)	1.6	0.40
ANP-800	800	27	90 (11)	3090	1.50	1.21 (0.55)	2.4	0.39
ANP-850	850	26	93 (10)	3010	1.62	1.16 (0.50)	3.7	0.35
ANP-900	900	19	96 (12)	2980	1.81	1.07 (0.46)	4.2	0.36
ANP-950	950	14	97 (11)	2640	1.71	0.91 (0.40)	7.6	0.33

^[a] The standard deviation is given in parenthesis.^[b] The pore volume of micropores < 1 nm is given in parenthesis.

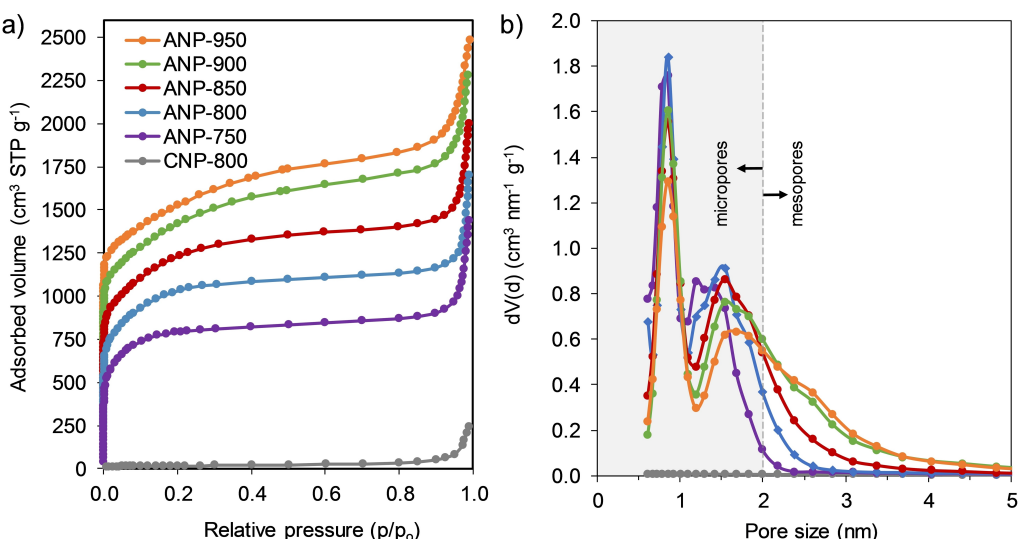


Figure 3. a) Nitrogen sorption isotherms and b) pore size distributions of the porous carbon nanoparticles. In panel a), the isotherms of ANP800, ANP-850, ANP-900, and ANP-950 are shifted up by 200, 400, 600, and 800 cm³ g⁻¹, respectively, for the sake of clarity.

another of larger micropores (1–2 nm) and small mesopores (2–4 nm). Moreover, it can be seen that the second pore system enlarges as the activation temperature increases, which can be related to additional carbon etching produced by the K₂CO₃ decomposition products (vide supra). TEM analysis further confirms the formation of larger micropores and small mesopores with the increase of the activation temperature (see Figure S2). The main textural characteristics (i.e., BET surface area, pore volume, and micropore volume) calculated for the PCNSs are listed in Table 1. The PCNSs have ultra-high BET surface areas, with values exceeding 3000 m² g⁻¹ for the samples activated at 750, 800, and 850 °C. Furthermore, these samples have large pore volumes (calculated for $p/p_0=0.9$), which increase steadily with temperature from 1.40 cm³ g⁻¹ (750 °C) to 1.81 cm³ g⁻¹ (900 °C). Activation at temperatures >900 °C (sample ANP-950) caused certain collapse of the microporous structure (see Figure 3b), which led to a decrease of all of the textural parameters (Table 1). The PCNSs are essentially microporous, with up to 83% of the total pore volume corresponding to the micropores (size < 2 nm), and up to 44% to the micropores < 1 nm (values corresponding to ANP-750, see Table 1). It should be noted that a KHCO₃/PPy weight ratio of 6 has been required for achieving such large pore developments in the PCNs. In fact, the sample activated at

800 °C using a lower weight ratio of 4.3 had a poorer pore development ($S_{\text{BET}}=2790 \text{ m}^2 \text{ g}^{-1}$, $V_p=1.32 \text{ cm}^3 \text{ g}^{-1}$, data not shown) than the ANP-800 nanoparticles synthesized using a weight ratio of 6.

The elemental composition of the nanoparticles is detailed in Table S1. The nanoparticles activated at 750 °C have a large oxygen content of 7.5 wt% as a consequence of the oxidative activation reactions. With the increase of the activation temperature, there is a progressive loss of oxygen due to the removal of thermally unstable moieties. This trend was corroborated by XPS measurements (Figure S4a and b). The quantitative analysis of the spectra indicates a decrease of the oxygen content from 5.7 at% in ANP-750 to 3.8 at% in ANP-950. Deconvolution of the C 1s peaks (Figure S4c and d) shows a progressive loss of all types of O functionalities with the increase of temperature, whilst deconvolution of the O 1s peaks (Figure S4e and f) does not reveal significant changes in oxygen speciation. It should be noted that, although the carbonized polypyrrole nanospheres have a high N content (12.3 wt% for sample CNP-800), activation brings about the almost complete removal of N-groups, which results in porous carbon samples with low nitrogen contents (0.3–1.2 wt%, see Table S1). Deconvolution of the N 1s peak from the sample activated at the lowest temperature (ANP-750) discloses that nitrogen is predominantly

pyrrolic-N (74% of total N, Figure S4g), in agreement with the nature of the carbon precursor, whilst the N 1s signal was not detected for ANP-950. The absence of any signal different than those of C 1s, O 1s and N 1s (see Figures S4a and b) confirms that the samples are free from any Fe or K impurity coming from the polymerization catalyst or the activating agent. EDX observation on every sample (results not shown) also confirms the efficiency of the washing step using only water.

The PCNSs exhibit good electrical conductivities with values that gradually increase with the activation temperature from 1.6 Scm^{-1} (750°C) to ca. 8 Scm^{-1} (950°C) (see Table 1). This rise in the electronic conductivity can be ascribed to the loss of electron-withdrawing oxygen heteroatoms and the progressive rearrangement of carbon atoms observed by Raman. Especially remarkable is the high conductivity of the sample produced at 950°C (3.8 wt% O), which is comparable to the values obtained for the carbon nanomaterials used as conductive additives in electrochemical devices (e.g., Super P: 8.6 Scm^{-1} , Ketjen black: 6.5 Scm^{-1} , or Super C65: 5.2 Scm^{-1}) and superior than the conductivities of commercial activated carbons used in supercapacitors (e.g., Supra 50: 4.3 Scm^{-1} or YP-50F: 1.1 Scm^{-1}). With regards to the packing densities of the PCNSs, they are in the $0.33\text{--}0.40 \text{ g cm}^{-3}$ range (see Table 1), which are consistent with the high pore development of these samples.

2.3. Electrochemical Properties of the Porous Carbon Nanoparticles

The activated carbon nanoparticles display several features that make them attractive for use as electroactive material in supercapacitors: i) a large specific area that provides a large number of ion adsorption sites; ii) short ion migration pathways that minimize diffusion resistance; and iii) a good electronic conductivity that promotes fast electron transport. Thus, a large energy storage capacity and fast response (i.e., high power) is expected from these materials. To test their electrochemical properties, symmetric cells were built using electrodes with a mass loading typical of commercial EDLC ($\sim 9\text{--}10 \text{ mg cm}^{-2}$ of active material). For a complete evaluation of the performance of the materials, cells were assembled using various electrolytes with different electrical conductivities and viscosities. The three electrolytes studied were $1 \text{ M H}_2\text{SO}_4$, 1 M TEABF_4 in AN, and EMImTFSI in AN (50/50 wt%), which allowed operational voltage windows of 1, 2.7 and 3 V, respectively.

The charge transport properties of the materials were first investigated by EIS analysis. Figure 4a collects the Nyquist plots obtained for the different activated nanoparticles and the commercial activated carbon YP-17D in the $1 \text{ M H}_2\text{SO}_4$ aqueous electrolyte. Remarkably, the plots for the ANP-based supercapacitors show a much shorter Warburg region in the medium frequency range compared to the YP-17D carbon, indicative of

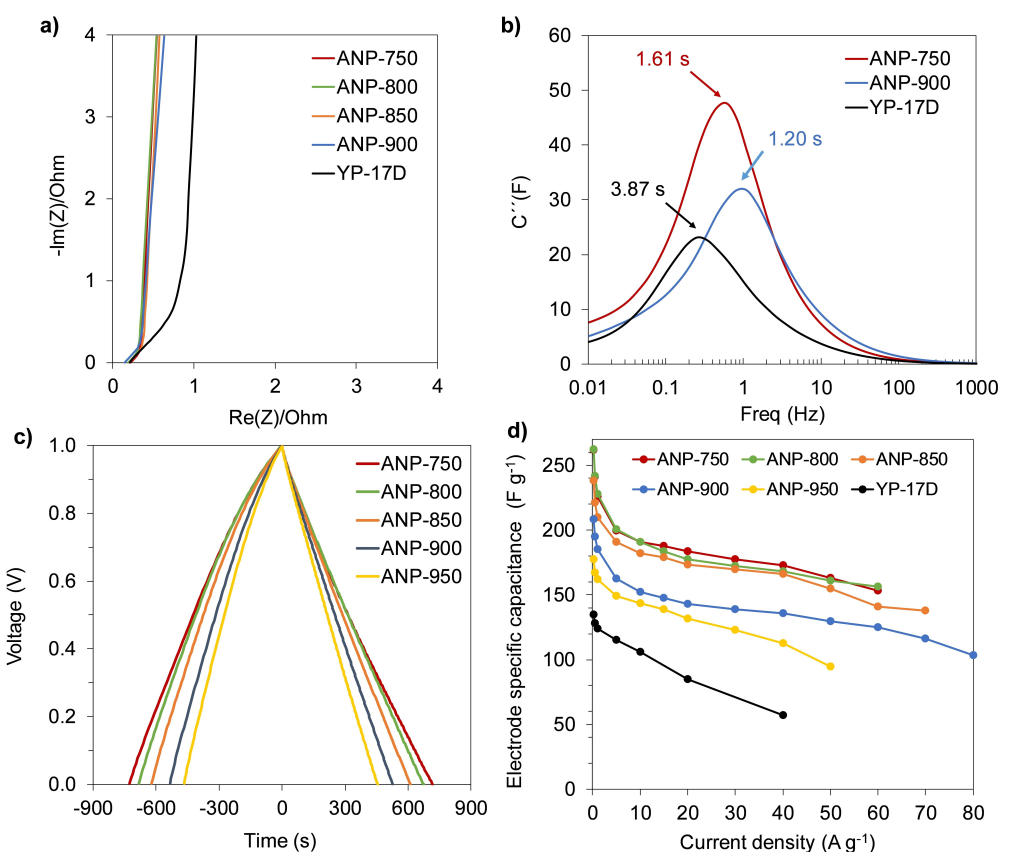


Figure 4. a) Nyquist plots for the symmetric cells tested in the aqueous electrolyte; b) Bode plots showing the calculation of the time constants; c) galvanostatic charge-discharge profiles recorded at a current density of 0.2 A g^{-1} and d) rate capability of the symmetric cells.

an easier diffusion of the electrolyte ions through their porosity. The calculated equivalent distributed resistance (EDR) of the commercial activated carbon is of 0.66 ohm, whilst the EDR of ANP-750 (the sample with the narrowest pores) is only of 0.12 ohm. This lower EDR in the activated nanoparticles is attributable to the short, readily accessible pores, whose length is limited by the small particle size (<100 nm). The relaxation time constant (τ_0), i.e., the minimum time required to reach half of the low-frequency capacitance, is considered as a factor of merit for supercapacitors.^[10] Its determination from the maximum of the imaginary part of the capacitance is depicted in Figure 4b. The YP-17D carbon has a time constant of 3.9 s, whilst the τ_0 calculated for the ANP-750 nanoparticles is as small as 1.6 s. For ANP-900, containing additionally some small mesopores, this value further decreases to 1.2 s, which anticipates an excellent response at fast charge-discharge rates for this material. The equivalent series resistance (ESR), calculated from the intersection of the plot with the X-axis at the highest frequency, decreases from 0.22 Ohm for ANP-750 to 0.15 ohm for ANP-900, in accordance with their respective electronic conductivities (see Table 1). The improved electron transport properties of the samples activated at higher temperatures is believed to further contribute (together with the widening of their porosity) to a better rate performance.

The charge storage capacity and rate capability of the materials were evaluated by means of galvanostatic charge-discharge cycling, as well as by cyclic voltammetry experiments. Figure 4c reveals that the charge-discharge profiles have a nearly triangular shape, confirming a pure electrical double layer mechanism. The excellent reversibility of the charge-discharge process is ratified by the high coulombic efficiencies that fall within the 98%–99% range. At the lowest current density studied (0.2 A g⁻¹), the ANP-750 sample achieves a large capacitance of 262 F g⁻¹. The ANP-800, ANP-850, ANP-900 and ANP-950 carbons achieve, respectively, 260, 240, 209, and 177 F g⁻¹ at the same current density. The increase in capacitance observed for lower activation temperatures can be attributed mainly to the larger micropore volumes (see Table 1), although improved wettability and some pseudocapacitance contribution from oxygen and nitrogen functionalities cannot be discarded. It has been demonstrated that capacitance is maximized when carbons contain narrow micropores with a size similar to that of the electrolyte ions (<1 nm).^[51,52] Particularly, the population of these narrow micropores in the nanoparticles decreases significantly for higher activation temperatures (Figure 3b). In fact, the calculated areal capacitance is highest for the ANP-750 carbon, reaching 8.6 μ F cm⁻², and decreases progressively down to 6.7 μ F cm⁻² for ANP-950, the sample with the widest pores.

The evolution of capacitance at increasing current rates is shown in Figure 4d. Within the whole range of current densities, the carbon nanoparticles perform better than the commercial activated carbon YP-17D from Kuraray, which achieves a maximum capacitance of 135 F g⁻¹ at 0.2 A g⁻¹ and fails at current densities over 40 A g⁻¹. The ANP-900 sample, which combines large micro- and mesopores, has the best rate performance and retains a capacitance above 100 F g⁻¹ at an

ultrahigh current density of 80 F g⁻¹ (a whole charge/discharge cycle took only 1.15 s). As discussed previously, activation at temperatures >900 °C leads to the partial collapse of the pore structure in ANP-950, which results in a poorer ion storage capacity and rate capability. Although the gravimetric capacitance is the most commonly used parameter in the scientific literature, the volumetric capacitance is regarded as more reliable to compare different materials with potential for actual use.^[53] As indicated in Figure S5, the commercial activated carbon has a high electrode packing density of 0.68 g cm⁻³, considerably higher than that of the ANP-750 nanoparticles, of 0.40 g cm⁻³. Nevertheless, the volumetric capacitance of the nanoparticles surpasses that of the commercial activated carbon due to their highly developed microporous structure with numerous adsorption sites, which results in a larger ion storage capacity for a given electrode volume. Thus, ANP-750 reaches a maximum volumetric capacitance of 89 F cm⁻³ at low current rates vs. 78 F cm⁻³ for YP-17D. The excellent rate capability of the carbon nanospheres is further confirmed by cyclic voltammetry experiments, in which these materials retain a quasi-rectangular shape at a fast scan rate of 500 mV s⁻¹, unlike the commercial activated carbon that shows a more resistive character (see Figure S6). The supercapacitors were run for 10000 charge-discharge cycles at a current density of 5 A g⁻¹ and showed a good long-term stability, experiencing capacity losses under 6% in all the cases at the end of the cycling tests (Figure S7).

The electrochemical performance of the nanoparticles was also evaluated in two high voltage organic electrolytes: 1 M TEABF₄ in AN and EMImTFSI in AN. The voltage plots recorded at 0.2 A g⁻¹ for the ANP-750 (most microporous) and ANP-900 (micro-mesoporous) carbons in the two organic electrolytes are shown in Figure 5a and b, respectively. The profiles are very close to an isosceles triangle, with coulombic efficiencies of 97%–98% in 1 M TEABF₄/AN and 95%–96% in EMImTFSI/AN, and the charge-discharge times are larger than those of YP-17D, which indicates a larger ion storage capacity. As with the aqueous H₂SO₄ electrolyte, ANP-750 achieves the highest capacitance in both organic electrolytes at low current rates, of 170–175 F g⁻¹, whilst the ANP-900 nanoparticles reach a maximum capacitance of 150–155 F g⁻¹. The values of areal capacitance are larger for ANP-750 (5.6 and 5.8 μ F cm⁻² in TEABF₄/AN and EMImTFSI/AN, respectively) than for ANP-900 (5.1 and 5.2 μ F cm⁻², respectively), what indicates a more efficient ion storage on the porous structure of ANP-750. On the other hand, the reference material YP-17D has a lower capacitance of 111 and 117 F g⁻¹ in 1 M TEABF₄/AN and EMImTFSI/AN, respectively. Compared to the aqueous H₂SO₄ electrolyte, the organic electrolytes are characterized by a lower conductivity, higher viscosity, and a larger ion size, all of these factors acting to the detriment of the rate performance of the cells. The Nyquist plots of the ANP-900-based supercapacitors in the three electrolytes studied (Figure S8) show a clear increase of both the equivalent and distributed series resistances for the organic electrolytes, as deduced from the right-shift of their intersection with the X-axis and the enlargement of their Warburg region, respectively. Nevertheless, the porous

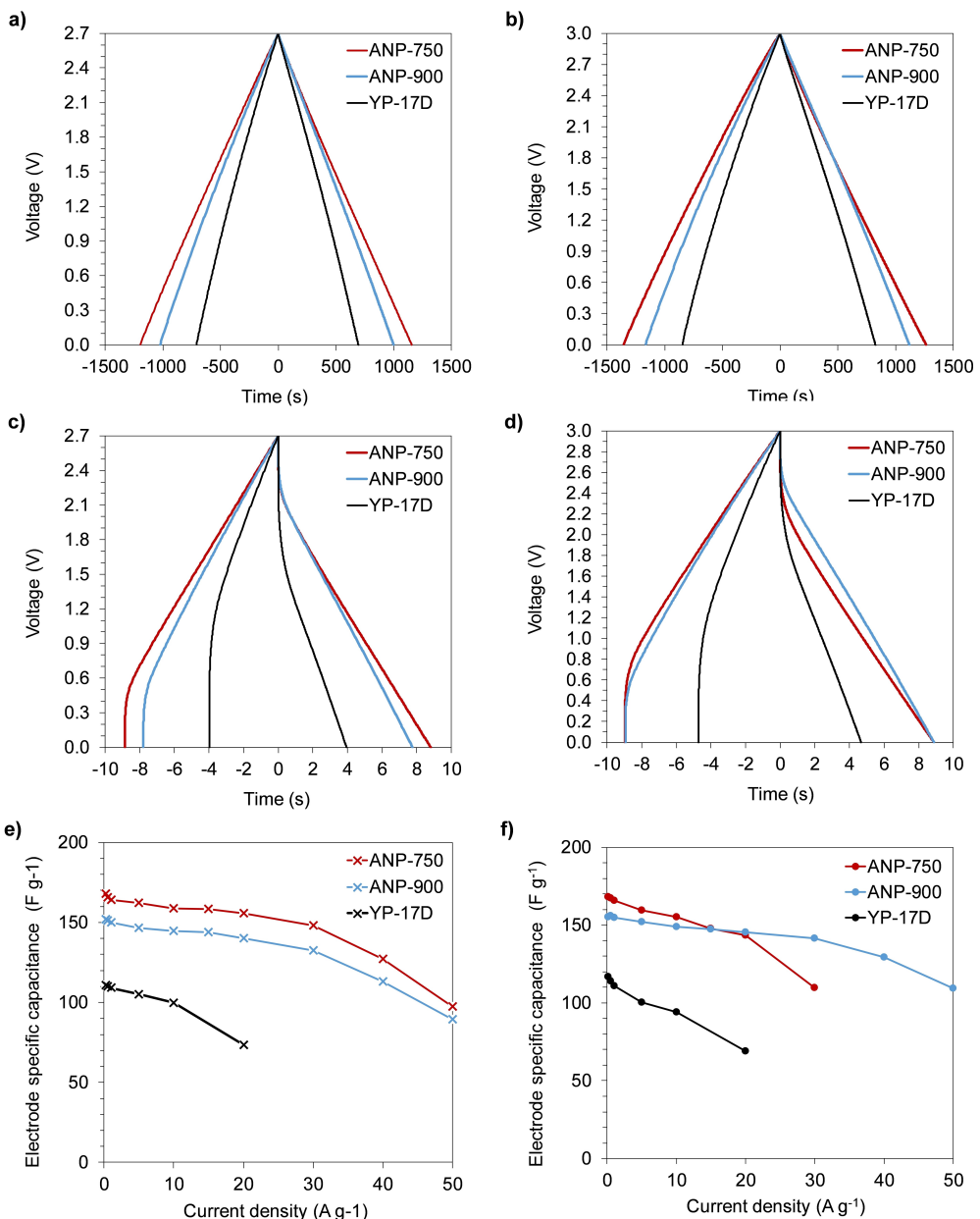


Figure 5. Voltage profiles showing the charge and discharge processes at a, b) 0.2 A g^{-1} and c, d) 20 A g^{-1} in the 1 M a, c) TEABF₄/AN and b, d) EMImTFSI/AN electrolytes. Rate capability of the supercapacitors in the 1 M e) TEABF₄/AN and f) EMImTFSI/AN electrolytes.

nano-particles retain well their capacitance, withstanding higher current densities than the commercial activated carbon (Figure 5c-f). Both materials show a good capacitance retention at 50 A g^{-1} (58% for ANP-750 and 59% for ANP-900) in the 1 M TEABF₄/AN electrolyte, as opposed to YP-17D that could be cycled only up to 20 A g^{-1} . In the case of the ionic liquid-based electrolyte, ANP-750 retains 66% of its maximum capacitance (110 F g^{-1}) at 30 A g^{-1} . This material could not be cycled at higher current densities, likely due to the similarity between the effective ion sizes of EMIm⁺ and TFSI⁻ in acetonitrile (~ 0.70 and 0.75 nm , respectively^[54]) and that of the small micropores present in this material. Thus, these ions can be correctly accommodated within the porosity of ANP-750 at low current rates, but there is a significant restriction to fast adsorption and

desorption at high current rates due to a size effect, as evidenced by the large IR drop observed in the voltage plot at 20 A g^{-1} (Figure 5d). This has been confirmed by EIS analysis, that reveals a relatively larger EDR and time constant for ANP-750 in EMImTFSI/AN compared to the micro-mesoporous ANP-900 (see Figure S9). In contrast, the ANP-900 nanoparticles could be charged and discharged up to a high current density of 50 A g^{-1} retaining 70% of its capacitance (109 F g^{-1}). The more favourable (wider) pore size distribution of this material favours the unrestrained sorption of the ionic liquid ions at fast rates, which allows taking full advantage of this high voltage electrolyte. The excellent values of capacitance and rate capability of the nanoparticles in the organic electrolytes were confirmed by cyclic voltammetry experiments (see Figure S10)

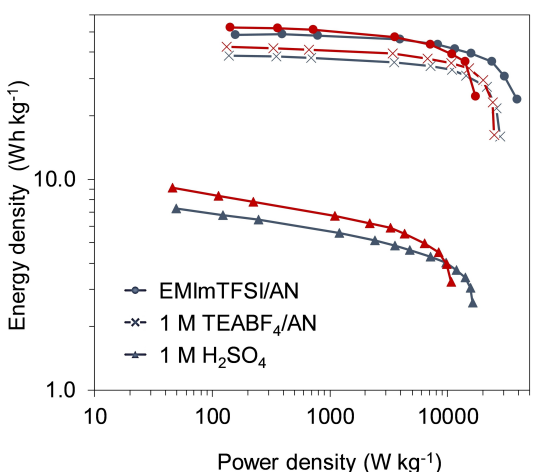


Figure 6. Ragone plots showing the energy and power densities of the symmetric capacitors built with the ANP-750 (red) and ANP-900 (blue) porous nanoparticles in the three tested electrolytes.

and compared favourably with those of other recently reported materials for high power capacitive systems, including carbon nanoparticles,^[20,55,56] microspheres,^[29,57,58] and hierarchically porous carbons^[59–62] (see Table S2). The cycling stability of the supercapacitors operating in the organic electrolytes was studied over 10000 cycles of charge-discharge at a current density of 10 A g^{-1} . The ANP-900 capacitors retain $>93\%$ of its initial capacitance in both organic electrolytes at the end of the cycling test (Figure S11). The supercapacitors built with ANP-750 carbon experience a larger capacitance decay with cycling (12%–14%), presumably due to the larger heteroatom content in the particles synthesized at lower temperature, which promotes certain degradation of the electrolyte at high operating voltages. This is specially evidenced in the case of the ionic liquid-based electrolyte, in which the ESR increased by 32% after the long-term cycling up to 3 V.

The large voltage achieved with the organic electrolytes (especially that of EMImTFSI/AN) allowed the storage of much more energy in the supercapacitors compared to the aqueous H_2SO_4 electrolyte. The Ragone plots showing the energy and power densities delivered by the ANP-750- and ANP-900-based systems are collected in Figure 6. ANP-750 achieves a maximum energy density of 42 Wh kg^{-1} in $1 \text{ M TEABF}_4/\text{AN}$ (current density = 0.2 A g^{-1}), retaining ca. 30 Wh kg^{-1} at a high power density of 20 kW kg^{-1} . In the EMImTFSI/AN electrolyte, the supercapacitors based on ANP-750 and ANP-900 store as much as 52 and 48 Wh kg^{-1} (current density = 0.2 A g^{-1}), respectively, the later delivering 31 Wh kg^{-1} at a high power density of 31 kW kg^{-1} . These results confirm the suitability of the porous nanoparticles for high power supercapacitors using a variety of electrolytes.

3. Conclusions

Monodisperse, highly porous carbon nanospheres have been successfully obtained by direct chemical activation of poly-pyrrole nanoparticles. The precursor polymeric nanoparticles

have a uniform size (diameter of ca. 110 nm) and they were produced through an easy synthetic pathway that involves the polymerization of pyrrole using FeCl_3 as oxidant. Subsequently, these particles were activated with a non-hazardous agent (KHCO_3), and the generated porous carbon nanoparticles were recovered simply by washing out the carbonized product with water. The resulting porous nanoparticles combine several important properties: i) uniform diameter (~95 nm with a standard deviation of around 10 nm); ii) ultra-high specific surface areas that surpassed $3000 \text{ m}^2 \text{ g}^{-1}$ with a porosity made up of micropores and small mesopores; and iii) high electronic conductivities (up to 7.6 Scm^{-1}). The nanoparticles were tested as electrodes in supercapacitors using mass loadings typical of commercial devices (ca. 10 mg cm^{-2}). They achieved high capacitance values in a variety of electrolytes: 262 , 168 and 155 Fg^{-1} at 0.2 A g^{-1} in $1 \text{ M H}_2\text{SO}_4$, $1 \text{ M TEABF}_4/\text{AN}$ and EMImTFSI/AN, respectively. Moreover, the unrestricted access of the electrolyte ions to the micropores allowed an excellent response when the PCNSs were tested under conditions of high-power demand, withstanding high current densities of 80 and 50 A g^{-1} in the aqueous and organic electrolytes, respectively.

Experimental Section

Synthesis of porous carbon nanoparticles

The polypyrrole nanoparticles were synthesized following the synthesis procedure reported by Lee et al.^[44] Briefly, 1.32 g of poly(vinyl alcohol) (MW 31000, Aldrich) was dissolved in distilled water (400 ml) under vigorous stirring for 30 min. Then, 29.9 g (184 mmol) of FeCl_3 (Aldrich) was added and the resulting PVA/ FeCl_3 solution was stirred at a speed of 350 rpm for 1 h. Subsequently, 2.55 g (38 mmol) of recently distilled pyrrole (Aldrich) was slowly added to the solution under continuous stirring. After 2 h of polymerization, the solid product was collected by centrifugation, washed several times with distilled water, and re-dispersed in water, and then, the water was removed by freeze-drying. The polymer nanoparticles were activated using potassium bicarbonate (Merck) using a KHCO_3/PPy weight ratio of 6 to guarantee large pore developments even at the lowest carbonization temperatures. To ensure a good mixing between both ingredients, firstly the KHCO_3 particles were dissolved in ~10 ml water and, subsequently, the PPy nanoparticles were dispersed in the solution under stirring. Afterwards, water was evaporated by heating under magnetic stirring, and the solid mixture was heat-treated up to a temperature of 750, 800, 850, 900 or 950°C under nitrogen gas flow (heating rate = 4°C min^{-1} and holding time = 1 h). The carbonized product was washed with distilled water for several hours and then, the porous nanoparticles were collected by filtration and dried at 120°C . The carbon samples were denoted as ANP-X, where X is the activation temperature. Carbonized nanoparticles were also synthesized by heat treatment of the polymeric nanoparticles at 800°C for 1 h (sample code: CNP-800).

Physicochemical characterization

Scanning electron microscopy (SEM) images were recorded by using a Quanta FEG650 (FEI) instrument, whereas transmission electron microscopy (TEM) images were acquired on a JEOL (JEM 2100-F) apparatus operating at 200 kV. The packing density and

electrical conductivity of the carbon powders were determined using a homemade apparatus in which the samples (~100 mg) are placed between two stainless steel plungers inside a hollow nylon cylinder with an inner diameter of 8 mm and subject to a load pressure of 7.1 MPa. The N₂ sorption isotherms of the carbon samples were measured at -196 °C using a Micromeritics ASAP 2020 sorptometer. The apparent surface area was calculated by the BET (Brunauer-Emmet-Teller) theory. The total pore volume was determined from the amount of nitrogen adsorbed at a relative pressure (p/p₀) of 0.90. The pore size distributions (PSDs) were determined by the quenched solid-state density functional theory (QSDFT) method for nitrogen. X-ray diffraction (XRD) patterns were acquired from a Siemens D5000 instrument operating at 40 kV and 20 mA, using a Cu K α radiation source. For the elemental analysis of the samples, a LECO CHN-932 microanalyzer was used. The Raman spectra were recorded on a Horiba (LabRam HR-800) spectrometer with a laser source of radiation that operated at a wavelength of 514 nm and a power of 25 mW. The X-ray photo-electron spectra (XPS) were acquired by a Specs apparatus which operated with a monochromatic Al radiation source at a voltage of 14.00 kV and a power of 175 W.

Electrochemical characterization

Electrodes were prepared by mixing 85 wt% of active material, 10 wt% of polytetrafluoroethylene (PTFE) binder (Aldrich, 60 wt% suspension in water), and 5% of carbon black Super C65 (Timcal) using several drops of ethanol. The slurries were kneaded to get a dough that was cut into disc-shaped electrodes with a diameter of 1 cm and an active material mass loading of ca. 10 mg cm⁻². The electrodes were then pressed to 4.5 tons, and their thickness was measured with the help of a micrometer to calculate their apparent density. The electrochemical measurements were carried out in two-electrode Swagelok™ type cells using 1 M H₂SO₄, 1 M TEABF₄/AN, and EMImTFSI/AN (1-Ethyl-3-methylimidazolium bis(trifluoromethylsulfonyl)imide, weight ratio of 1:1) (99%, Ionic Liquids Technology, Germany) as the electrolyte solutions. The electrodes were electrically isolated by glassy fibrous separators. A commercial activated carbon, Kuraray YP-17D, was also measured for comparison purposes. Electrochemical impedance spectroscopy (EIS), cyclic voltammetry (CV) and galvanostatic charge/discharge (CD) experiments were performed at room temperature using a computer-controlled potentiostat (Bio-Logic VMP3 multichannel generator). EIS curves were obtained within the 1 mHz–100 kHz frequency range. Cyclic voltammetry experiments were conducted using a cell voltage of 1 V for 1 M H₂SO₄, 2.7 V for 1 M TEABF₄/AN, and 3 V for EMImTFSI/AN at increasing sweep rates from 1 mV s⁻¹ to 500 mV s⁻¹. Plots of electrode specific capacitance (expressed in Farads per gram of active material) vs. cell voltage were calculated using Equation (1):

$$C_{\text{el}} = 4 \frac{I}{v m}, \quad (1)$$

where I is the current (A), v is the scan rate (V s⁻¹) and m is the total mass (g) of active material in the supercapacitor. Galvanostatic charge/discharge cycling was carried out using the same cell voltages as in the CV experiments at increasing current densities from 0.2 to 80 A g⁻¹, based on the mass of active material in one electrode. The specific gravimetric capacitance of the electrodes (F g⁻¹) was determined from the galvanostatic discharge branches using Equation (2):

$$C_{\text{el}} = 4C = 4 \frac{I}{\left(\frac{dV}{dt}\right)m}, \quad (2)$$

where C is the cell capacitance and dV/dt is the slope of the discharge curve. As most supercapacitors are operated in the range of V_{max} to approximately $1/2 V_{\text{max}}$ the upper half of the discharge curve was used to determine the slope of the discharge curve. The values of volumetric capacitance were calculated considering the apparent density of the electrodes and the mass fraction of active material, according to Fuertes et al.^[63] To trace the Ragone-like plots, the specific energy (Wh kg⁻¹) and power (kW kg⁻¹) densities were calculated using Equations (3) and (4):

$$E = \frac{1}{2} C \Delta V^2 = \frac{1}{8} C_{\text{el}} \Delta V^2 \quad (3)$$

$$P = \frac{E}{\Delta t_d}, \quad (4)$$

where ΔV is the operating voltage ($V_{\text{max}} - IR_{\text{drop}}$) and Δt_d is the discharge time. Long-term cycling stability was evaluated by continuous galvanostatic charge/discharge cycling over 10000 cycles. The cycling was performed at a current density of 5 A g⁻¹ for the aqueous electrolyte and 10 A g⁻¹ for 1 M TEABF₄/AN and EMImTFSI/AN.

Supporting Information

Supporting Information is available from the Wiley Online Library or from the author.

Acknowledgements

This research work was supported by projects RTI2018-093712-B-I00 (MCIU/AEI/FEDER, UE) and IDI/2018/000148 (regional GRUPIN2018).

Conflict of Interest

The authors declare no conflict of interest.

Keywords: high power • high surface area • microporous materials • nanoparticles • supercapacitors

- [1] L. Wang, X. Hu, *Chem. Asian J.* **2018**, *13*, 1518.
- [2] W. J. Liu, H. Jiang, H. Q. Yu, *Energy Environ. Sci.* **2019**, *12*, 1751.
- [3] H. Shao, Y. C. Wu, Z. Lin, P. L. Taberna, P. Simon, *Chem. Soc. Rev.* **2020**, *49*, 3005.
- [4] J. Wang, X. Zhang, Z. Li, Y. Ma, L. Ma, *J. Power Sources* **2020**, *451*, 227794.
- [5] M. Xu, Q. Yu, Z. Liu, J. Lv, S. Lian, B. Hu, L. Mai, L. Zhou, *Nanoscale* **2018**, *10*, 21604.
- [6] H. Tian, T. Wang, F. Zhang, S. Zhao, S. Wan, F. He, G. Wang, *J. Mater. Chem. A* **2018**, *6*, 12816.
- [7] S. Chen, Q. Kuang, H. J. Fan, *Small* **2020**, *16*, 1.

- [8] R. Hou, B. Liu, Y. Sun, L. Liu, J. Meng, M. D. Levi, H. Ji, X. Yan, *Nano Energy* **2020**, *72*, 104728.
- [9] L. Yang, J. Shui, L. Du, Y. Shao, J. Liu, L. Dai, Z. Hu, *Adv. Mater.* **2019**, *31*, 1.
- [10] F. Beguin, E. Frackowiak, *Carbons for Electrochemical Energy Storage and Conversion Systems*, CRC Press, Boca Raton, FL, USA **2009**.
- [11] A. B. Fuertes, P. Tartaj, *Small* **2007**, *3*, 275.
- [12] Z. Wang, F. Li, A. Stein, *Nano Lett.* **2007**, *7*, 3223.
- [13] Z. Sun, Y. Liu, B. Li, J. Wei, M. Wang, Q. Yue, Y. Deng, S. Kaliaguine, D. Zhao, *ACS Nano* **2013**, *7*, 8706.
- [14] G. Wang, Y. Sun, D. Li, H.-W. Liang, R. Dong, X. Feng, K. Müllen, *Angew. Chem.* **2015**, *127*, 15406.
- [15] J. Liu, T. Yang, D. W. Wang, G. Q. Lu, D. Zhao, S. Z. Qiao, *Nat. Commun.* **2013**, *4*, 1.
- [16] C. Long, L. Miao, D. Zhu, H. Duan, Y. Lv, L. Li, M. Liu, L. Gan, *ACS Appl. Energ. Mater.* **2021**, *4*, 5727.
- [17] J. Liu, S. Z. Qiao, H. Liu, J. Chen, A. Orpe, D. Zhao, G. Q. Lu, *Angew. Chem. Int. Ed.* **2011**, *50*, 5947.
- [18] S. Wang, W. C. Li, G. P. Hao, Y. Hao, Q. Sun, X. Q. Zhang, A. H. Lu, *J. Am. Chem. Soc.* **2011**, *133*, 15304.
- [19] S. Wang, W. C. Li, L. Zhang, Z. Y. Jin, A. H. Lu, *J. Mater. Chem. A* **2014**, *2*, 4406.
- [20] V. K. Tiwari, Z. Chen, F. Gao, Z. Gu, X. Sun, Z. Ye, *J. Mater. Chem. A* **2017**, *5*, 12131.
- [21] Z. Chen, Z. Ye, Z. Chen, Z. Ye, *Gen. Chem.* **2019**, *5*, 180023.
- [22] M. M. Titirici, M. Antonietti, *Chem. Soc. Rev.* **2010**, *39*, 103.
- [23] M. Sevilla, J. B. Parra, A. B. Fuertes, *ACS Appl. Mater. Interfaces* **2013**, *5*, 6360.
- [24] M. Sevilla, A. B. Fuertes, *ChemSusChem* **2016**, *9*, 1880.
- [25] M. Sevilla, P. Valle-Vigón, A. B. Fuertes, *Adv. Funct. Mater.* **2011**, *21*, 2781.
- [26] A. S. Mestre, C. Freire, J. Pires, A. P. Carvalho, M. L. Pinto, *J. Mater. Chem. A* **2014**, *2*, 15337.
- [27] X. Li, Y. Song, L. You, L. Gao, Y. Liu, W. Chen, L. Mao, *Ind. Eng. Chem. Res.* **2019**, *58*, 2933.
- [28] F. Su, C. K. Poh, J. S. Chen, G. Xu, D. Wang, Q. Li, J. Lin, X. W. Lou, *Energy Environ. Sci.* **2011**, *4*, 717.
- [29] N. Díez, M. Sevilla, A. B. Fuertes, *ChemElectroChem* **2020**, *7*, 3798.
- [30] N. Díez, M. Sevilla, A. B. Fuertes, *ACS Appl. Energ. Mater.* **2020**, *3*, 3397.
- [31] J. Ludwinowicz, M. Jaroniec, *Carbon* **2015**, *82*, 297.
- [32] G. A. Ferrero, N. Díez, M. Sevilla, A. B. Fuertes, *ACS Appl. Energ. Mater.* **2018**, *1*, 6560.
- [33] W. H. Lee, J. H. Moon, *ACS Appl. Mater. Interfaces* **2014**, *6*, 13968.
- [34] K. Ai, Y. Liu, C. Ruan, L. Lu, G. Lu, *Adv. Mater.* **2013**, *25*, 998.
- [35] B. Friedel, S. Greulich-Weber, *Small* **2006**, *2*, 859.
- [36] X. Zhang, S. K. Manohar, *J. Am. Chem. Soc.* **2005**, *127*, 14156.
- [37] Z. Liu, X. Zhang, S. Poyraz, S. P. Surwade, S. K. Manohar, *J. Am. Chem. Soc.* **2010**, *132*, 13158.
- [38] J. Jang, H. Yoon, *Chem. Commun.* **2003**, *3*, 720.
- [39] J. Jang, J. H. Oh, *Chem. Commun.* **2004**, *4*, 882.
- [40] J. Jang, H. Yoon, *Small* **2005**, *1*, 1195.
- [41] O. S. Kwon, J. Y. Hong, S. J. Park, Y. Jang, J. Jang, *J. Phys. Chem. C* **2010**, *114*, 18874.
- [42] J. Y. Hong, H. Yoon, J. Jang, *Small* **2010**, *6*, 679.
- [43] X. Ning, W. Zhong, S. Li, L. Wan, *Mater. Lett.* **2014**, *117*, 294.
- [44] S. Lee, K. Y. Shin, J. Jang, *Nanoscale* **2015**, *7*, 9646.
- [45] M. Sevilla, N. Díez, A. B. Fuertes, *ChemSusChem* **2021**, *14*, 94.
- [46] D. W. McKee, *Fuel* **1983**, *62*, 170.
- [47] J. Hayashi, T. Horikawa, I. Takeda, K. Muroyama, F. Nasir Ani, *Carbon* **2002**, *40*, 2381.
- [48] N. Díez, G. A. Ferrero, A. B. Fuertes, M. Sevilla, *Batteries & Supercaps* **2019**, *2*, 701.
- [49] M. Sevilla, G. A. Ferrero, A. B. Fuertes, *Chem. Mater.* **2017**, *29*, 6900.
- [50] M. Sevilla, G. A. Ferrero, N. Díez, A. B. Fuertes, *Carbon* **2018**, *131*, 193.
- [51] J. Chmiola, G. Yushin, Y. Gogotsi, C. Portet, P. Simon, P. L. Taberna, *Science* **2006**, *313*, 1760.
- [52] N. Jackel, P. Simon, Y. Gogotsi, V. Presser, *ACS Energy Lett.* **2016**, *1*, 1262.
- [53] Y. Gogotsi, P. Simon, *Science* **2011**, *334*, 917.
- [54] R. Lin, P. Huang, J. Ségalini, C. Largeot, P. L. Taberna, J. Chmiola, Y. Gogotsi, P. Simon, *Electrochim. Acta* **2009**, *54*, 7025.
- [55] Z. Liu, Z. Zhou, W. Xiong, Q. Zhang, *Langmuir* **2018**, *34*, 10389.
- [56] X. Hao, J. Wang, B. Ding, Z. Chang, Y. Wang, H. Dou, X. Zhang, *ChemNanoMat* **2017**, *3*, 895.
- [57] J. K. Kim, Y. Yoo, Y. C. Kang, *Chem. Eng. J.* **2020**, *382*, 122805.
- [58] S. Feng, Z. Liu, Q. Yu, Z. Zhuang, Q. Chen, S. Fu, L. Zhou, L. Mai, *ACS Appl. Mater. Interfaces* **2019**, *11*, 4011.
- [59] N. Díez, G. A. Ferrero, M. Sevilla, A. B. Fuertes, *J. Mater. Chem. A* **2019**, *7*, 14280.
- [60] H. Zhang, X. He, F. Wei, S. Dong, N. Xiao, J. Qiu, *ACS Sustainable Chem. Eng.* **2020**, *8*, 3065.
- [61] S. Li, X. Song, X. Wang, C. Xu, Y. Cao, Z. Xiao, C. Qi, M. Wu, Z. Yang, L. Fu, X. Ma, J. Gao, *Carbon* **2020**, *160*, 176.
- [62] A. Khan, R. Arumugam Senthil, J. Pan, Y. Sun, X. Liu, *Batteries & Supercaps* **2020**, *3*, 731.
- [63] A. B. Fuertes, G. A. Ferrero, M. Sevilla, *Energy Storage Mater.* **2016**, *4*, 154.

Manuscript received: July 16, 2021

Revised manuscript received: October 25, 2021

Accepted manuscript online: October 28, 2021

Version of record online: November 10, 2021